Experimental Section

Synthesis of La-VS_{2-x}

3 mmol $Na_3VO_4 \cdot 12H_2O$ and 15 mmol C_2H_5NS were dissolved in 40 mL of deionized water, and then 0.05 mM $La_2(CO_3)_3 \cdot 8H_2O$ was added under stirring for 10 min. Afterwards, a piece of carbon cloth (CC, 1 cm × 2 cm) was transferred to a Teflon-lined stainless-steel autoclave and kept at 170 °C for 24 h. The obtained La-VS_{2-x} grown on CC was washed with deionized water and ethanol several times. For comparison, pristine VS_2 grown on CC was prepared by the same procedure without addition of $La_2(CO_3)_3 \cdot 8H_2O$.

Electrochemical measurements

Electrochemical measurements were carried out on a CHI-660E electrochemical workstation using a standard three-electrode system. The Ag/AgCl, graphite rod, and catalyst coated on CC (1 × 1 cm^2) were used as reference electrode, counter electrode, and working electrode, respectively. All potentials were referenced to reversible hydrogen electrode (RHE) according to the equation: E (V vs. RHE) = E (V vs. Ag/AgCl) + 0.198 V + 0.059 × pH. The NO_3RR measurements were carried out in Ar-saturated 0.5 M Na_2SO_4 + 0.1 M KNO_3 electrolyte using an H-type two-compartment electrochemical cell separated by a Nafion 211 membrane. The Nafion membrane was pretreated by heating it in 5% H_2O_2 aqueous solution at 80 °C for 1 h and then in deionized water at 80 °C for another 1 h. After each chronoamperometry test for 1 h, the produced NH_3 and other possible by-products (NO_2^- and N_2H_4) were analyzed by various colorimetric methods using UV-vis absorbance spectrophotometer (MAPADA P5), while the gas products (H_2, N_2) were analyzed by gas chromatography (Shimadzu GC2010). The detailed determination procedures are given in our previous publication[1].

Calculations of NH_3 yield rate and NH_3-Faradaic efficiency

$$\text{NH}_3 \text{ yield rate } (\mu\text{g h}^{-1} \text{ mg}_{\text{cat.}}^{-1}) = \frac{c_{\text{NH}_3} \times V}{t \times A} \quad (1)$$

$$\mathrm{NH_3\text{-}Faradaic\ efficiency}\ (\%) = \frac{8 \times F \times c_{\mathrm{NH_3}} \times V}{17 \times Q} \times 100\% \quad (2)$$

where c_{NH3} (μg mL^{-1}) is the measured NH_3 concentration, V (mL) is the volume of the electrolyte, t (h) is the reduction time, A (cm^{-2}) is the surface area of CC (1×1 cm^2) , F (96500 C mol^{-1}) is the Faraday constant, Q (C) is the quantity of applied electricity.

Characterizations

Transmission electron microscopy (TEM) and high-resolution transmission electron microscopy (HRTEM) were carried out on a Tecnai G^2 F20 microscope. X-ray diffraction (XRD) pattern was conducted on a Rigaku D/max 2400 diffractometer. Scanning electron microscopy (SEM) was carried out on a ZEISS GeminiSEM-500 microscope. Electron paramagnetic resonance (EPR) measurements were conducted on a Bruker ESP-300 spectrometer.

Calculation details

Spin-polarized DFT calculations were performed using a Cambridge sequential total energy package (CASTEP). The exchange-correlation interactions were modeled by using Perdew–Burke–Ernzerhof (PBE) generalized gradient approximation (GGA) functional. The description of van der Waals interactions was based on a DFT-D correction method. During the geometry optimization, a cutoff energy of 450 eV was used and the convergence tolerance was set to be 1.0×10^{-5} eV for energy and 0.02 eV Å^{-1} for force. The Brillouin zone was sampled by 3×3×1 Monkhorst−Pack k-point mesh. The VS_2 (001) was modeled by a 4×4 supercell, and a vacuum region of 15 Å was used to separate adjacent slabs. The adsorption energy (ΔE) is calculated as[2]

$$\Delta E = E_{\mathrm{ads/slab}} - E_{\mathrm{ads}} - E_{\mathrm{slab}} \quad (3)$$

where $E_{ads/slab}$, E_{ads} and E_{slab} are the total energies for adsorbed species on slab, adsorbed species and isolated slab, respectively.

The computational hydrogen electrode (CHE) model was adopted to calculate the Gibbs free energy change (ΔG) for each elementary step as follows:

$$\Delta G = \Delta E + \Delta ZPE - T\Delta S \quad (4)$$

where ΔE is the adsorption energy, ΔZPE is the zero-point energy difference and $T\Delta S$ is the entropy difference between the gas phase and adsorbed state. The entropies of

free gases were acquired from the NIST database. Given that it is difficult to directly calculate the energy of charged NO_3^-, the adsorption free energy of NO_3^- ($\Delta G(*NO_3)$) was calculated with assistance of the gaseous HNO_3 as follows[3]

$$\Delta G(*NO_3) = G(*NO_3) - G(*) - [G(HNO_3) - 0.5 \times G(H_2)] + \Delta G_{correct} \quad (5)$$

where $G(*)$ and $G(*NO_3)$ are the Gibbs free energies of the bare catalyst and that with the adsorbed NO_3^-, respectively. $G(HNO_3)$ and $G(H_2)$ represent the Gibbs free energies of HNO_3 and H_2 molecule, respectively.

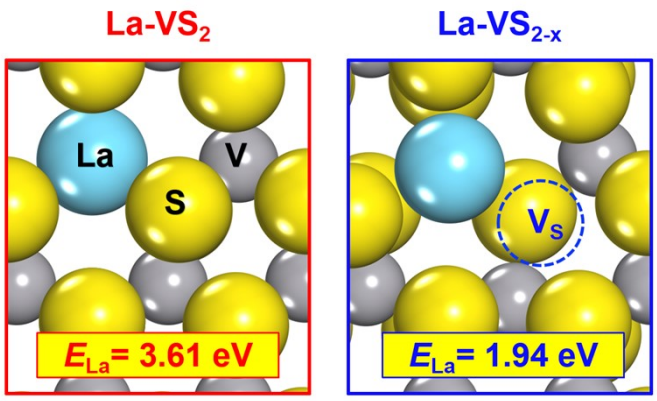

Fig. S1. La-dopant formation energy (E_{La}) of V_S-free La-VS_2 and V_S-containing La-VS_{2-x}.

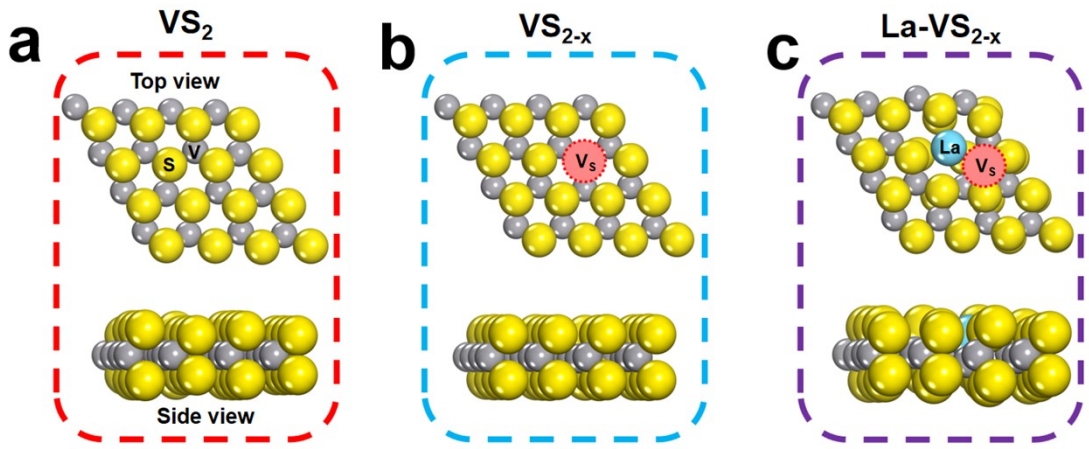

Fig. S2. Atomic structures of VS_2, VS_{2-x} and La-VS_{2-x}.

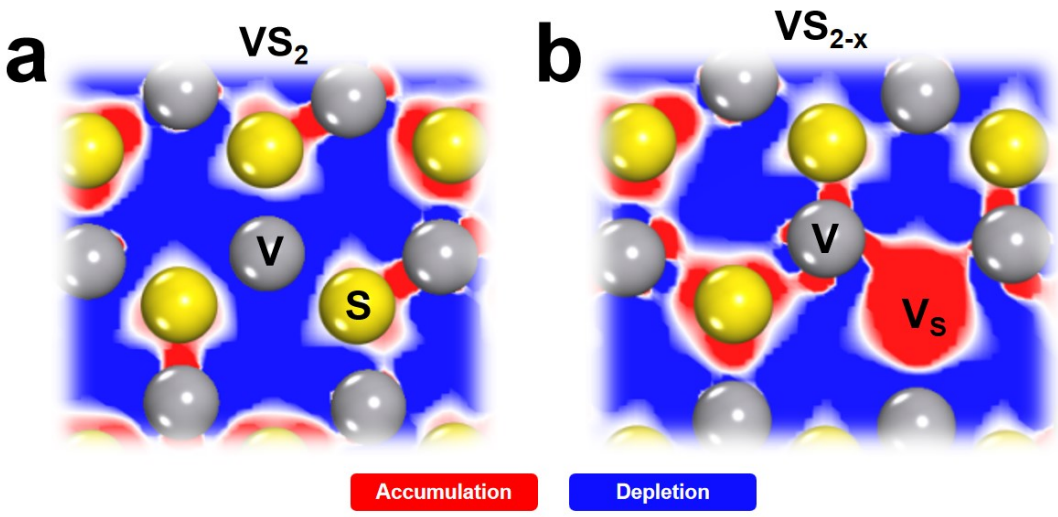

Fig. S3. Electron contour maps of (a) VS_2 and (b) VS_{2-x}.

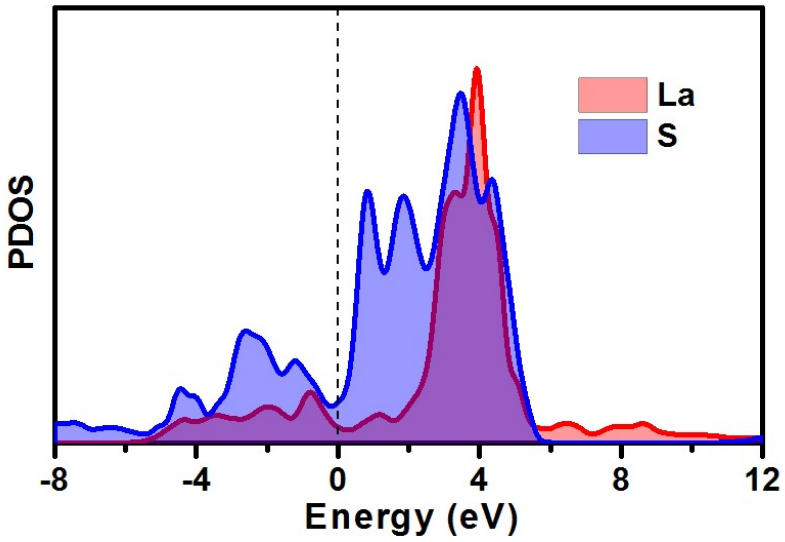

Fig. S4. PDOS plot of La/S orbital hybridization in La-VS_{2-x}.

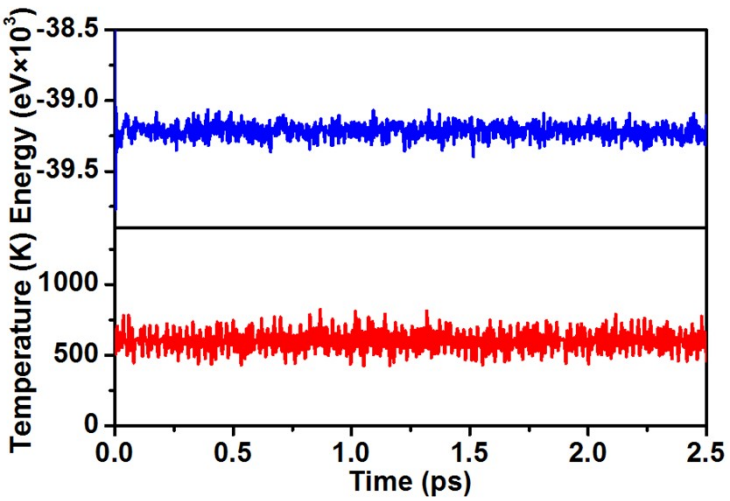

Fig. S5. Variations of energy and temperature during the AIMD simulation for assessing the thermodynamic stability of La-VS_{2-x} (inset: geometric structure of La-VS_{2-x} after AIMD simulation).

It is seen that both energy and temperature keep the equilibrium states at 600 K, confirming the high thermodynamic stability of La-VS_{2-x}.

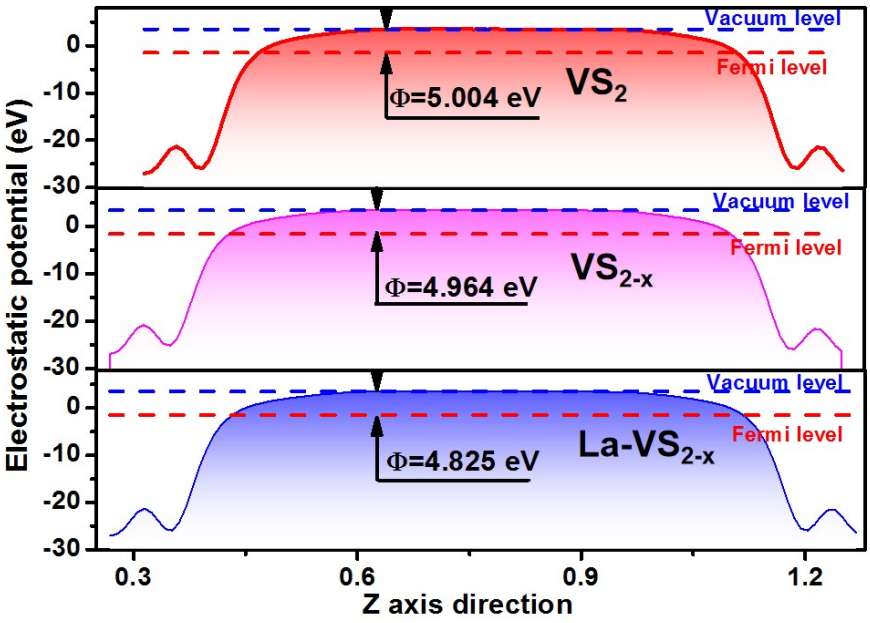

Fig. S6. Average potential profiles along c-axis direction for calculating the work functions (Φ) of VS_2, VS_{2-x} and La-VS_{2-x}.

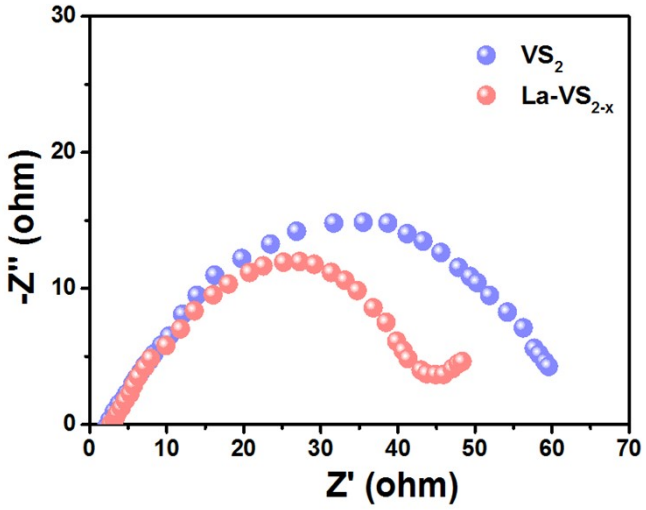

Fig. S7. Electrochemical impendence spectra of VS_2 and La-VS_{2-x}.

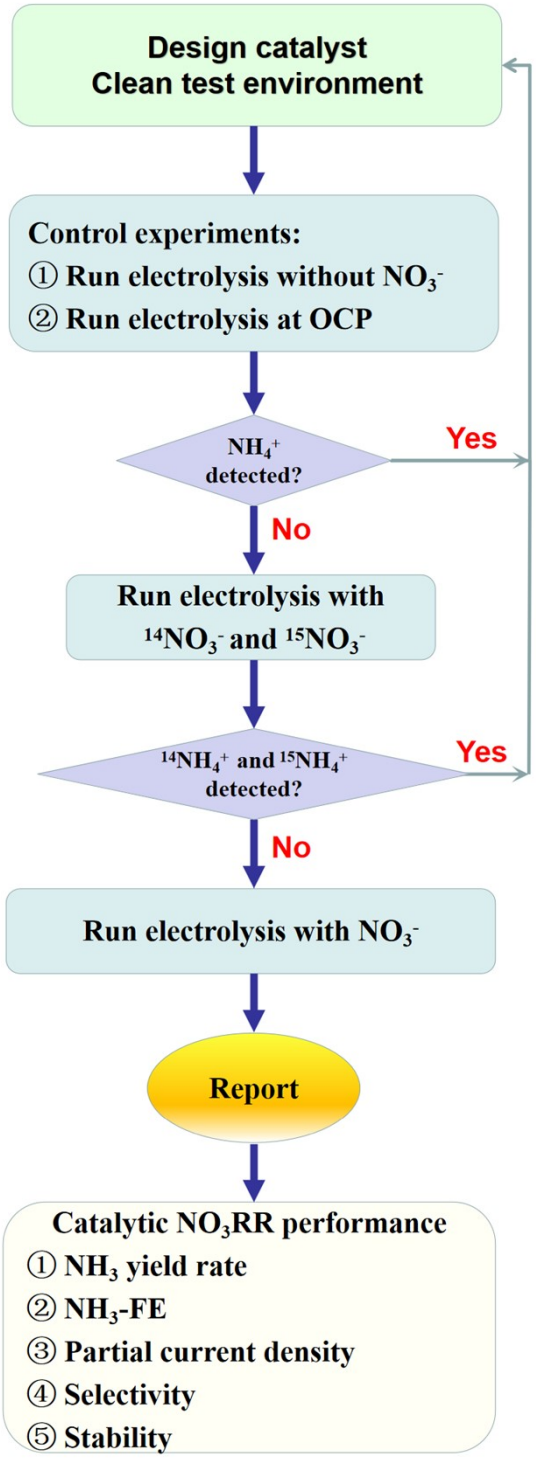

Fig. S8. Flow chart of the electrocatalytic NO_3RR measurement procedure.

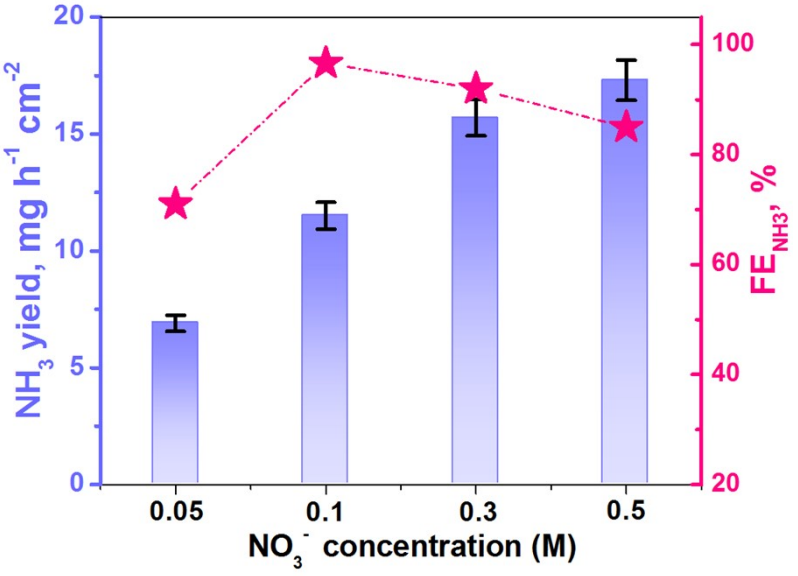

Fig. S9. NH_3 yield rates and FE_{NH3} of La-VS_{2-x} at different nitrate concentrations.

We investigate the influence of starting nitrate concentration on the NO_3RR performance of La-VS_{2-x}. It is seen in Fig. S9 that NH_3 yield rate is monotonously increased with increasing nitrate concentration, while FE_{NH3} peaks at 0.1 M. As FE_{NH3} is commonly regarded as a more important indicator than NH_3 yield rate for NH_3 electrosynthesis, we take 0.1 M as the optimum nitrate concentration for our NO_3RR measurements. The reduced FE_{NH3} beyond 0.1 M can be due presumably to the adverse effects of expedited competing HER at lower nitrate concentration (0.05 M) and plentiful NO_3^- occupying the active sites at higher nitrate concentration (0.3~0.5 M)[4].

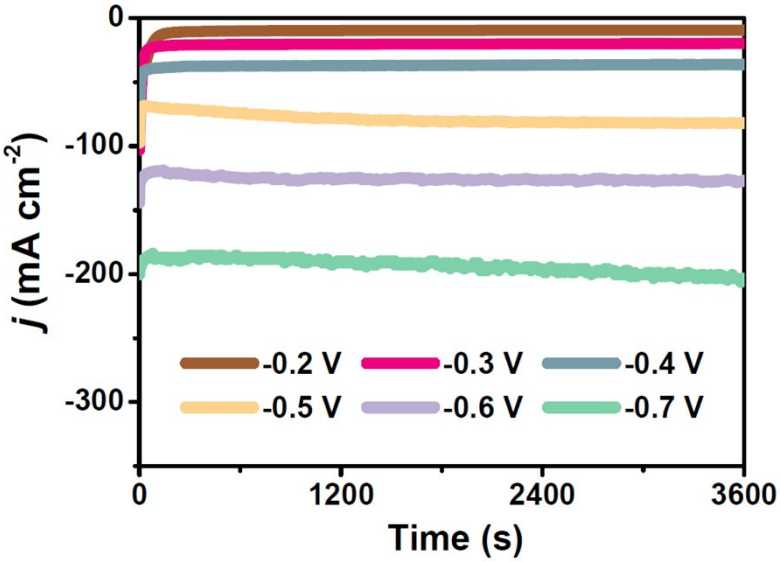

Fig. S10. Potential-dependent chronoamperometry curves of La-VS_{2-x} after 1 h of NO_3RR electrolysis.

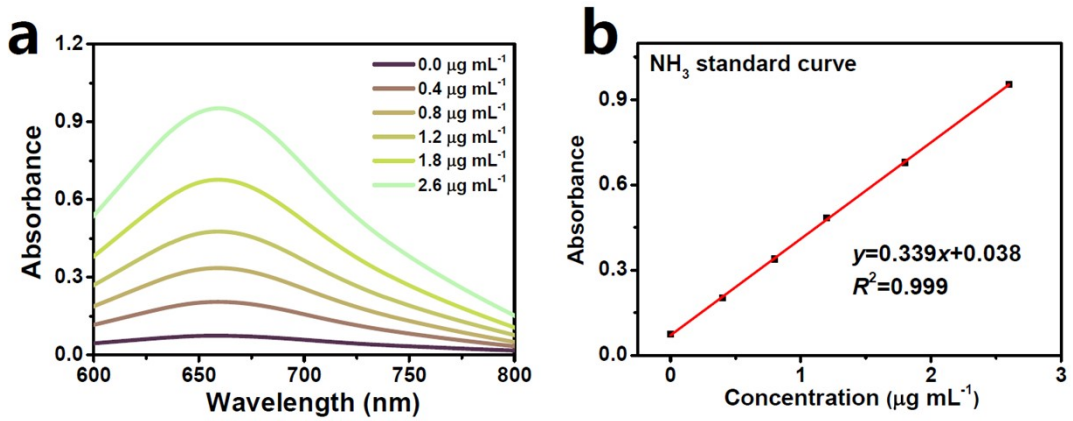

Fig. S11. (a) UV-vis absorption spectra of NH_4Cl assays after incubated for 2 h at ambient conditions. (b) Calibration curve used for the calculation of NH_3 concentrations.

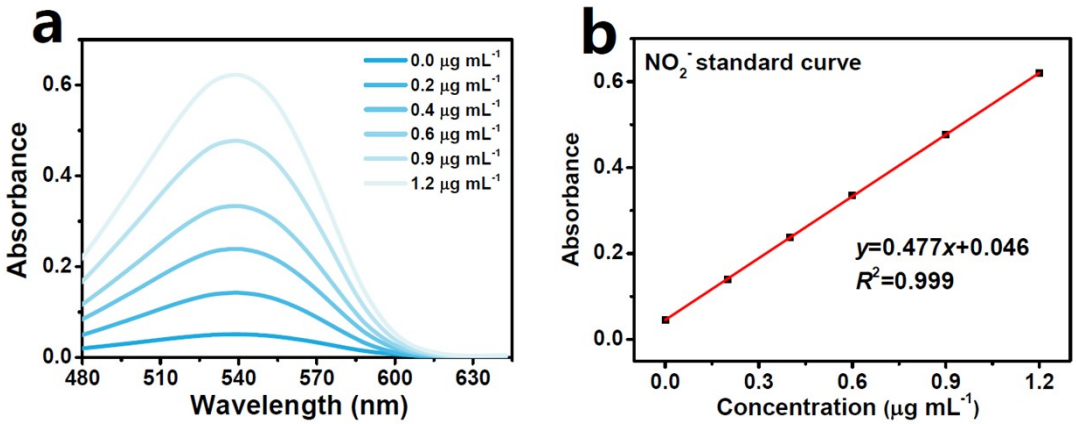

Fig. S12. (a) UV-vis absorption spectra of KNO_2 assays after incubated for 20 min at ambient conditions. (b) Calibration curve used for calculation of NO_2^- concentrations.

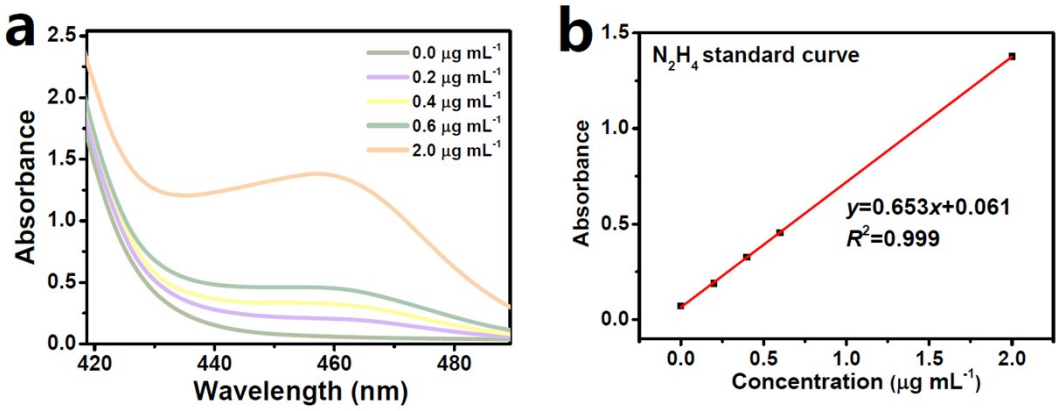

Fig. S13. (a) UV-vis absorption spectra of N_2H_4 assays after incubated for 20 min at ambient conditions. (b) Calibration curve used for calculation of N_2H_4 concentrations.

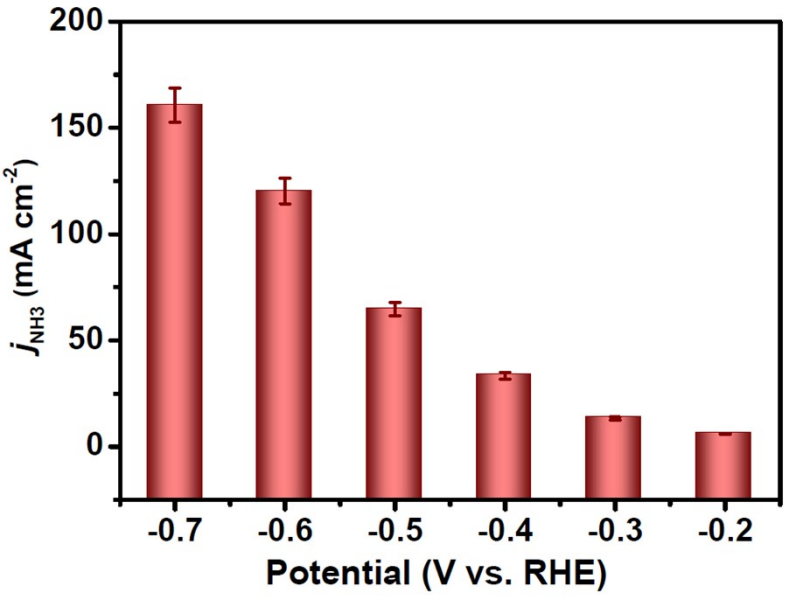

Fig. S14. Calculated NH_3 partial current densities of La-VS_{2-x} at various potentials.

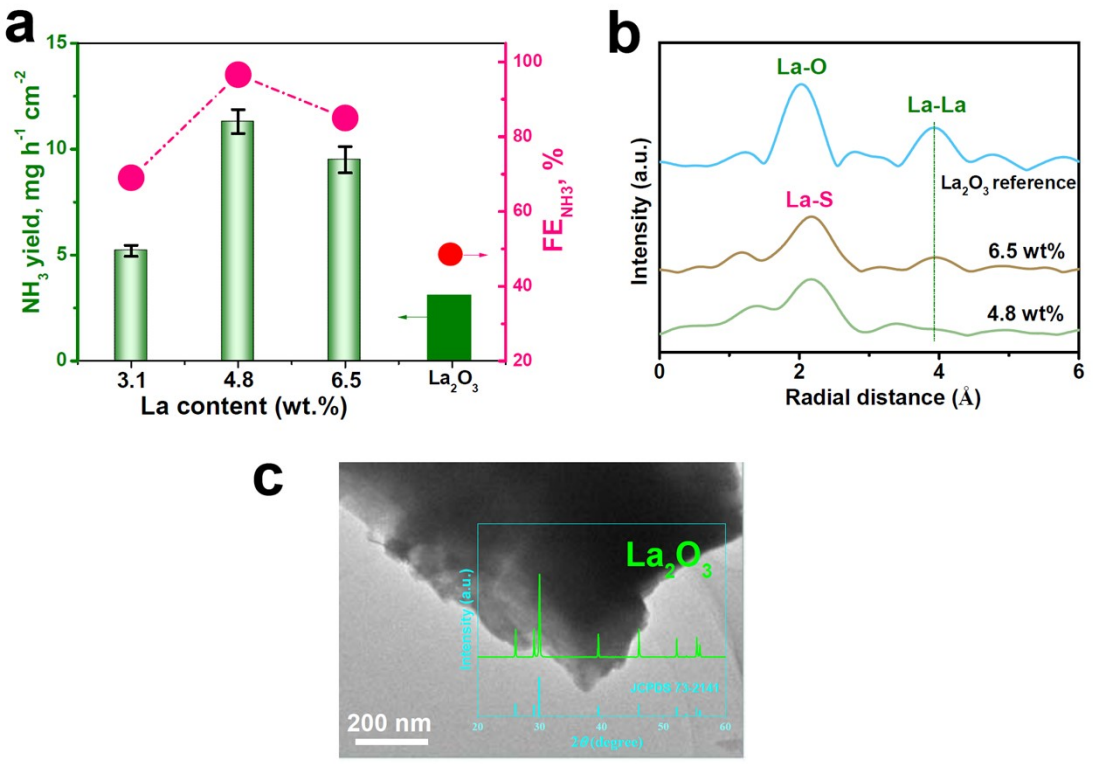

Fig. S15. (a) NO_3RR performances of La-VS_{2-x} with different La contents (3.1-6.5 wt%) at -0.6 V. (b) EXAFS spectra of 4.8 and 6.5 wt% La-VS_{2-x} and La_2O_3 reference. (c) TEM image and XRD pattern (inset) of La_2O_3 nanoplates, which was prepared by a reported method[5].

It is seen in Fig. S15a that the NO_3RR performance of La-VS_{2-x} peaks at 4.8 wt%, whereas the lower (3.1 wt%) and higher (6.5 wt%) La contents lead to the distinct performance degradation. The poor performance of 3.1 wt% La-VS_{2-x} can be explained by the insufficient single-atom La active sites, while the reduced performance of 6.5 wt% La-VS_{2-x} can be attributed possibly to the formation of La_2O_3 species due to the excessive La addition, as evidenced by the EXAFS spectra (Fig. S15b) where 6.5 wt% La-VS_{2-x} shows the characteristic La-La bond of La_2O_3 reference. To verify this, we prepare La_2O_3 nanoplates (Fig. S15c) which exhibits a very poor NO_3RR property (Fig. S15a). Hence, the presence of NO_3RR-unfavored La_2O_3 species on 6.5 wt% La-VS_{2-x} is the main cause for its decreased performance. Therefore, the abundant atomically dispersed La-dopants involved in 4.8 wt% La-VS_{2-x} contribute to the highest NO_3RR performance.

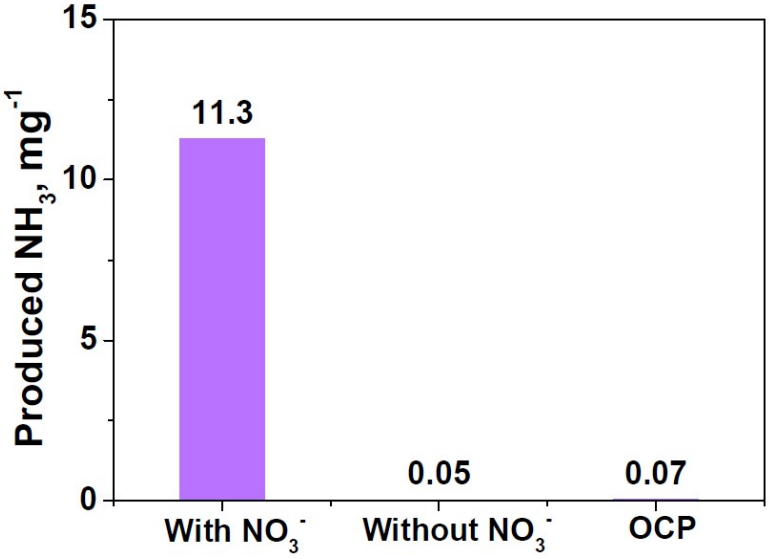

Fig. S16. Amounts of produced NH_3 under different conditions: electrolysis in NO_3^--containing electrolyte at −0.6 V; electrolysis in NO_3^--free electrolyte at -0.6; electrolysis in NO_3^--containing electrolyte at open-circuit potential (OCP).

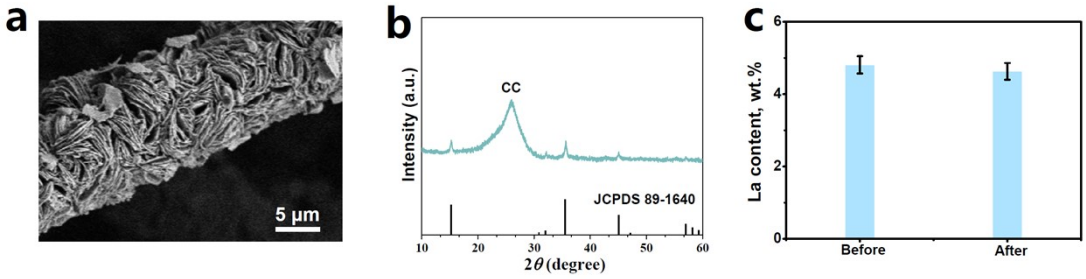

Fig. S17. (a) SEM image, (b) XRD pattern and (c) La content of La-VS_{2-x} after stability tests.

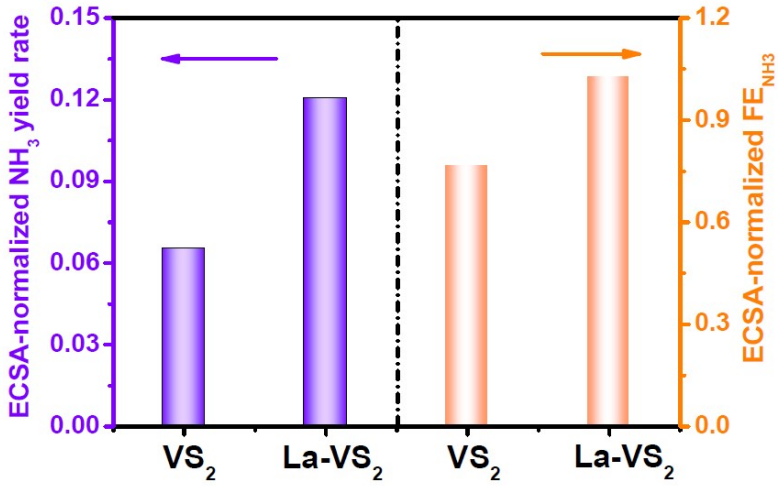

Fig. S18. ECSA-normalized NH_3 yield rates and FE_{NH3} of VS_2 and La-VS_{2-x} at -0.6 V.

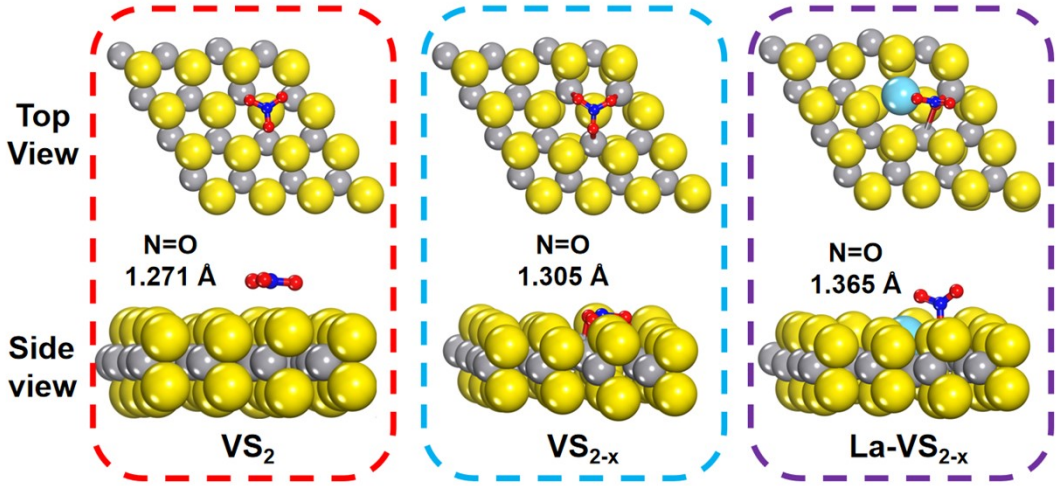

Fig. S19. Optimized atomic configurations of NO_3^- adsorption on VS_2, VS_{2-x} and La-VS_{2-x}.

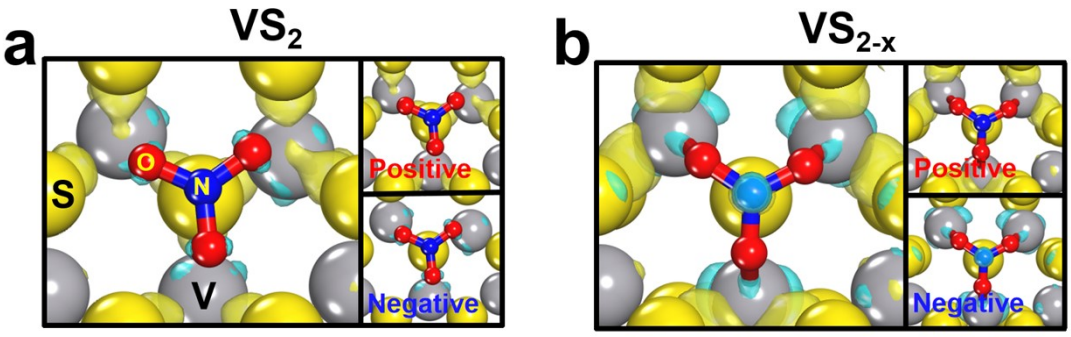

Fig. S20. Differential charge density maps of NO_3^- adsorption on (a) VS_2 and (b) VS_{2-x} (yellow: accumulation, cyan: depletion).

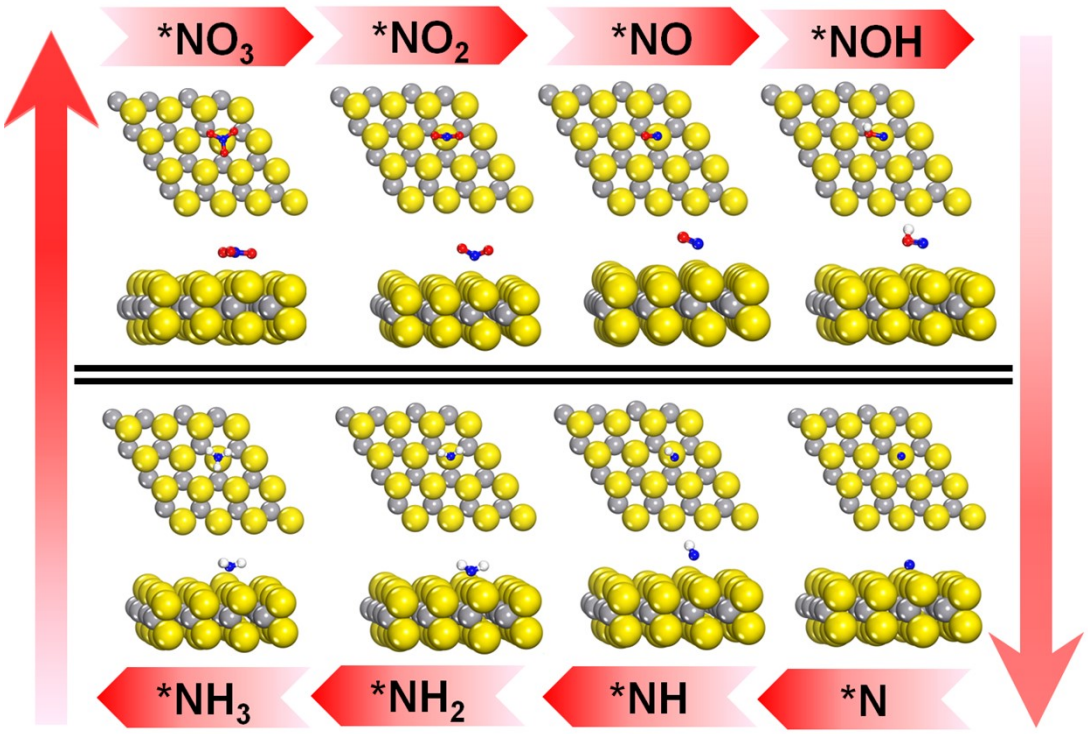

Fig. S21. Optimized atomic configurations of NO_3RR intermediates on VS_2.

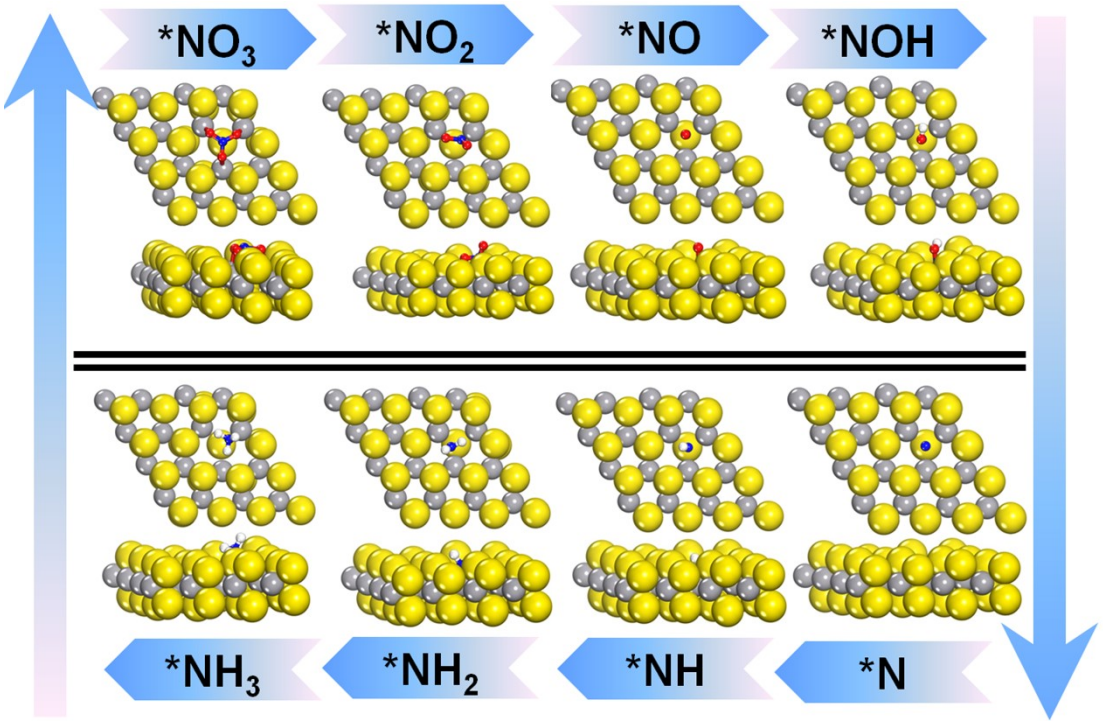

Fig. S22. Optimized atomic configurations of NO_3RR intermediates on VS_{2-x}.

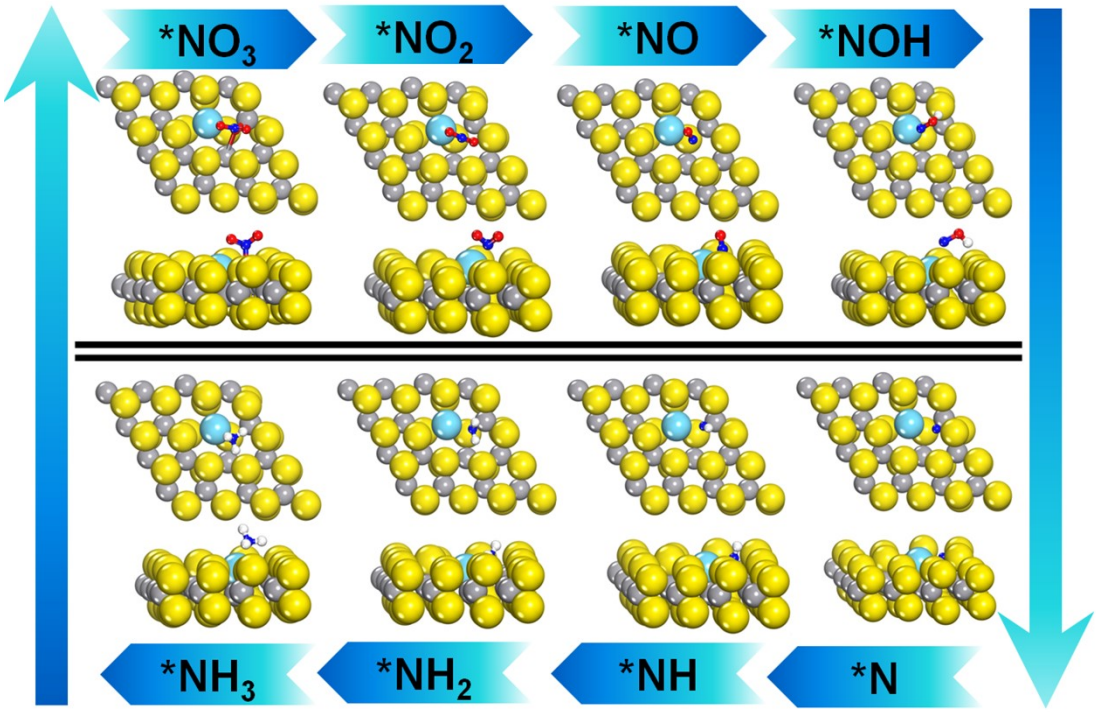

Fig. S23. Optimized atomic configurations of NO_3RR intermediates on La-VS_{2-x}.

Table S1. Structural parameters extracted from the La L_3-edge EXAFS fitting.

Sample	Shell	CN	R (Å)	σ^2 (10^{-3}Å)	ΔE_0 (eV)	R factor (%)
La-VS_{2-x}	La-S	5.2	2.47	8.5	-3.7	0.012

CN is the coordination number; R is interatomic distance; σ^2 is Debye-Waller factor; ΔE_0 is edge-energy shift; R factor is used to value the goodness of the fitting.

Table S2. Comparison of the optimum NH_3 yield and FE_{NH3} for the recently reported state-of-the-art NO_3RR electrocatalysts at ambient conditions.

Catalyst	Electrolyte	NH_3 yield rate (mg $h^{-1}cm^{-2}$)	FE_{NH3}(%)	Potential (V vs RHE)	Ref.
Fe_3O_4/SS	0.1 M NaOH (0.1 M $NaNO_3$)	10.15	91.5	-0.5	[6]
Co_2AlO_4/CC	0.1 M PBS （0.1 M NO_3^-）	7.9	92.6	-0.7	[7]
$ZnCo_2O_4$ NSA/CC	0.1 M NaOH （0.1 M $NaNO_3$）	10.79	98.33	-0.6	[8]
PdCoO/NF	0.5 M K_2SO_4 （200 mg/LNO_3^-）	3.47	88.6	-1.3	[9]
Poly-Cu_{14}cba	0.5 M K_2SO_4 （250 ppm NO_3^-）	2.84	90	-0.15	[10]
Pd nanocrystalline	0.1 M Na_2SO_4 （0.1 M NO_3^-）	9.32	79.91	-0.7	[11]
a-RuO_2	0.5 M Na_2SO_4 (200 ppm NO_3^-)	1.97	97.46	-0.35	[12]
Rh@Cu	0.1 M Na_2SO_4 0.1 M KNO_3	13.57	93	−0.2	[13]
Cu–PTCDA	1 M PBS （500 ppm KNO_3）	0.44	85.9	-0.4	[14]
CoO@NCNT /GP	0.1 M NaOH 0.1 M $NaNO_3$	9.04	93.8	−0.6	[15]
TiO_2 NTs/CuO_x	0.5 M Na_2SO_4 100 ppm KNO_3	1.24	92.23	−0.75	[16]
Co–P/TP	0.2 M Na_2SO_4 （200 ppm NO_3^-）	0.42	93.6 ±3.3	-0.3	[17]
Cu_3P NA/CF	0.1 M PBS （0.1 M $NaNO_2$）	1.63	91.2±2.5	-0.5	[18]
La-VS_{2-x}	0.1 M Na_2SO_4 0.1 M $NaNO_3$	11.3	96.6	−0.6	This work

Supplementary references

[1]. K. Chen, Y. Luo, P. Shen, X. Liu, X. Li, X. Li and K. Chu, *Dalton Trans.*, 2022, **51**, 10343-10350.

[2]. A. A. Peterson, F. Abild-Pedersen, F. Studt, J. Rossmeisl and J. K. Nørskov, *Energy Environ. Sci.*, 2010, **3**, 1311-1315.

[3]. D. Wu, P. Lv, J. Wu, B. He, X. Li, K. Chu, Y. Jia and D. Ma, *J. Mater. Chem. A*, 2023, **11**, 1817-1828.

[4]. Y. Wang, H. Li, W. Zhou, X. Zhang, B. Zhang and Y. Yu, *Angew. Chem. Int. Edit.*, 2022, **134**, e202202604.

[5]. B. Xu, Z. Liu, W. Qiu, Q. Liu, X. Sun, G. Cui, Y. Wu and X. Xiong, *Electrochim. Acta*, 2018, **298**, 106-111.

[6]. X. Fan, L. Xie, J. Liang, Y. Ren, L. Zhang, L. Yue, T. Li, Y. Luo, N. Li, B. Tang, Y. Liu, S. Gao, A. A. Alshehri, Q. Liu, Q. Kong and X. Sun, *Nano Res.*, 2021, **15**, 3050–3055.

[7]. Z. Deng, J. Liang, Q. Liu, C. Ma, L. Xie, L. Yue, Y. Ren, T. Li, Y. Luo, N. Li, B. Tang, A. A. Alshehri, I. Shakir, P. O. Agboola, S. Yan, B. Zheng, J. Du, Q. Kong and X. Sun, *Chem. Eng. J.*, 2022, **435**, 135104.

[8]. Z. Li, J. Liang, Q. Liu, L. Xie, L. Zhang, Y. Ren, L. Yue, N. Li, B. Tang, A. A. Alshehri, M. S. Hamdy, Y. Luo, Q. Kong and X. Sun, *Mater. Today Phys.*, 2022, **23**, 100619.

[9]. M. Liu, Q. Mao, K. Shi, Z. Wang, Y. Xu, X. Li, L. Wang and H. Wang, *ACS Appl. Mater. Interfaces*, 2022, **14**, 13169-13176.

[10]. Y. M. Wang, J. Cai, Q. Y. Wang, Y. Li, Z. Han, S. Li, C. H. Gong, S. Wang, S. Q. Zang and T. C. Mak, *Angew. Chem., Int. Ed.*, 2022, **134**, e202114538.

[11]. Y. Han, X. Zhang, W. Cai, H. Zhao, Y. Zhang, Y. Sun, Z. Hu, S. Li, J. Lai and L. Wang, *J. Colloid Interf. Sci.*, 2021, **600**, 620-628.

[12]. Y. Wang, H. Li, W. Zhou, X. Zhang, B. Zhang and Y. Yu, *Angew. Chem., Int. Ed.*, 2022, **134**, e202202604.

[13]. H. Liu, X. Lang, C. Zhu, J. Timoshenko, M. Rüscher, L. Bai, N. Guijarro, H. Yin, Y. Peng, J. Li, Z. Liu, W. Wang, B. R. Cuenya and J. Luo, *Angew. Chem., Int. Ed.*, 2022, **61**, e202202556.

[14]. G.-F. Chen, Y. Yuan, H. Jiang, S.-Y. Ren, L.-X. Ding, L. Ma, T. Wu, J. Lu and H. Wang, *Nat. Energy*, 2020, **5**, 605-613.

[15]. Q. Chen, J. Liang, L. Yue, Y. Luo, Q. Liu, N. Li, A. A. Alshehri, T. Li, H. Guo and X. Sun, *Chem. Commun.*, 2022, **58**, 5901-5904.

[16]. W. Qiu, X. Chen, Y. Liu, D. Xiao, P. Wang, R. Li, K. Liu, Z. Jin and P. Li, *Appl. Catal., B*, 2022, **315**, 121548.

[17]. Z. Li, G. Wen, J. Liang, T. Li, Y. Luo, Q. Kong, X. Shi, A. M. Asiri, Q. Liu and X. Sun, *Chem. Commun.*, 2021, **57**, 9720-9723.

[18]. J. Liang, B. Deng, Q. Liu, G. Wen, Q. Liu, T. Li, Y. Luo, A. A. Alshehri, K. A. Alzahrani and D. Ma, *Green Chem.*, 2021, **23**, 5487-5493.